SPACE-TIME VISUALIZATION OF DYNAMICS IN LAGRANGIAN COHERENT STRUCTURES OF TIME-DEPENDENT 2D VECTOR FIELDS

Sven Bachthaler[1], Filip Sadlo[1], Carsten Dachsbacher[2] and Daniel Weiskopf[1]
[1]*VISUS, University of Stuttgart, Stuttgart, Germany*
[2]*Karlsruhe Institute of Technology, Karlsruhe, Germany*

Keywords: Flow Visualization, Lagrangian Coherent Structures, Hyperbolic Trajectories.

Abstract: Lagrangian coherent structures (LCS), apparent as ridges in the finite-time Lyapunov exponent (FTLE) field, represent a time-dependent alternative to the concept of separatrices in vector field topology. Traditionally, LCS are analyzed and visualized in terms of their geometric shape only, neglecting stretching and compression in tangent directions. These effects are, however, of particular interest in mixing phenomena and turbulence. Hyperbolicity plays an important role in these processes and gives rise to hyperbolic trajectories originating at the intersections of forward and reverse LCS. Since integration of hyperbolic trajectories is difficult, we propose to visualize the corresponding space-time intersection curves of LCS instead. By stacking the traditional 2D FTLE video frames of time-dependent vector fields, a space-time FTLE field is obtained. In this field, ridge lines turn into ridge surfaces representing LCS, and their intersection forms curves that are a robust alternative to hyperbolic trajectories. Additionally, we use a space-time representation of the time-dependent vector field, leading to a steady 3D space-time vector field. In this field, the LCS become stream surfaces given that their advection property is sufficiently met. This makes visualization of the dynamics within LCS amenable to line integral convolution (LIC), conveying in particular the dynamics around hyperbolic trajectories. To avoid occlusion, the LCS can be constrained to space-time bands around the intersection curves, resembling visualization by saddle connectors. We evaluate our approach using synthetic, simulated, and measured vector fields.

1 INTRODUCTION

As science and engineering methods evolve, modeling of phenomena is shifting from stationary to time-dependent domains. 2D computational fluid dynamics (CFD) simulations are of major importance in several domains, such as the analysis of flow in films and on free-slip boundaries. To examine and understand such data, efficient tools for analysis and visualization are required. Feature extraction techniques, providing a condensed representation of the essential information, are often applied to the visualization of vector fields. A prominent concept revealing the overall structure is vector field topology (Helman and Hesselink, 1989). Whereas vector field topology is directly applicable only to steady or quasi-stationary vector fields, Lagrangian coherent structures (LCS) (Haller, 2001) are popular for the analysis of time-dependent vector fields. LCS are a time-dependent counterpart to separatrices, which are streamlines started from separating regions of different behavior. LCS have been increasingly subject to research in the last decade and can be obtained as maximizing curves (ridges) in the finite-time Lyapunov exponent (FTLE), a scalar field measuring the separation of trajectories (Haller, 2001). FTLE computation is, however, an expensive task because at least one trajectory needs to be computed per sample point. LCS behave as material lines under the action of time-dependent flow, i.e., they are advected and exhibit negligible cross-flow for sufficiently long advection time intervals, as reported by Haller (Haller, 2001), Lekien et al. (Lekien et al., 2005), and Sadlo et al. (Sadlo et al., 2012). This property gives rise, e.g., to the acceleration technique by Sadlo et al. (Sadlo et al., 2011) based on grid advection.

Our new method adopts the concept of hyperbolic trajectories and space-time streak manifolds, which we therefore discuss in the following. Previous work by Sadlo and Weiskopf (Sadlo and Weiskopf, 2010)

Bachthaler S., Sadlo F., Dachsbacher C. and Weiskopf D..
SPACE-TIME VISUALIZATION OF DYNAMICS IN LAGRANGIAN COHERENT STRUCTURES OF TIME-DEPENDENT 2D VECTOR FIELDS.
DOI: 10.5220/0003810905730583
In *Proceedings of the International Conference on Computer Graphics Theory and Applications* (IVAPP-2012), pages 573-583
ISBN: 978-989-8565-02-0

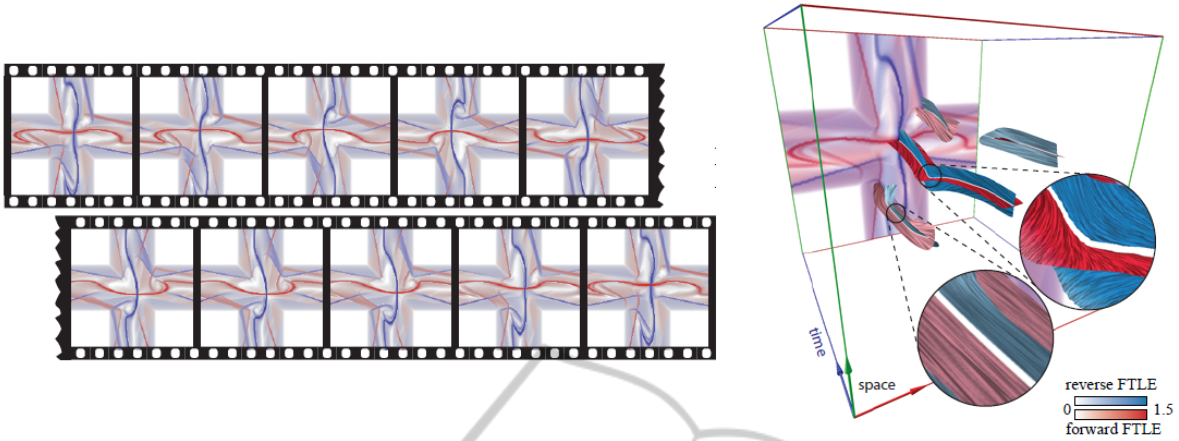

Figure 1: Left: traditional visualization of a time-dependent vector field by time series of the finite-time Lyapunov exponent is difficult to analyze and does not convey the dynamics inside its ridges (Lagrangian coherent structures). Right: our space-time representation reveals the overall structure and makes the dynamics inside the Lagrangian coherent structures visible by line texture patterns. Close-ups: in contrast to the traditional 2D visualization, different dynamics along intersection curves (almost parallel flow on the left vs. strongly hyperbolic flow on the right) is apparent.

generalized vector field topology to time-dependent vector fields by replacing the role of streamlines by generalized streak lines (Wiebel et al., 2007). This way, critical points turn into degenerate streak lines and separatrices into streak lines (space-time streak manifolds) converging toward these degenerate streak lines in forward or reverse time. It was found that these need to be distinguished degenerate streak lines identical to the previously discovered hyperbolic trajectories (Haller, 2000).

Hyperbolic trajectories can be seen as constituent structures in time-dependent 2D vector field topology. As mentioned, space-time streak manifolds—the time-dependent counterpart to separatrices—can be constructed alone from hyperbolic trajectories—no dense sampling is required in contrast to the FTLE approach. However, a major limitation with hyperbolic trajectories is the difficulty of their integration. Although the integration error tends to grow exponentially in linear vector fields, it is usually negligible due to comparably short advection times and low separation rates along common trajectories. Unfortunately, this is not the case in typical hyperbolic configurations due to large separation rates and the fact that both forward and reverse integration are subject to repulsion from one of the LCS (see Fig. 2). Hyperbolic trajectories coincide with the intersection of forward and reverse LCS; since ridges in forward FTLE represent repelling LCS whereas those in reverse FTLE are attracting, the trajectory is repelled from the former forward and from the latter in backward direction.

Our method has therefore a twofold objective: (1) avoiding the integration of hyperbolic trajectories by replacing them with intersections of LCS, and (2) revealing tangential dynamics in LCS, accomplished by line integral convolution (LIC). By treating time as an additional dimension, we obtain a stationary visualization that conveys the overall structure in space-time. Several approaches for obtaining seeds for hyperbolic trajectories exist: by intersecting ridges in hyperbolicity time (Haller, 2000), ridges in FTLE (Sadlo and Weiskopf, 2010), and constructing streak manifolds from them, or by building a time-dependent linear model from critical points (Ide et al., 2002). This kind of visualization of hyperbolic trajectories is, however, restricted to LCS geometry, i.e., the dynamics in the vicinity of the hyperbolic trajectories is not conveyed. Furthermore, the hyperbolicity of the vector field is typically analyzed by requiring negative determinant of the velocity gradient. This approach fails in providing insight into the role and importance of hyperbolic trajectories. In contrast, our LIC-based visualization captures the configuration of the flow in the neighborhood of hyperbolic trajectories and also in general along LCS. One example is the discrimination of almost parallel flow configurations from strongly hyperbolic ones (Fig. 1, (right)). This provides increased insight in the overall dynamics, interplay, and importance of LCS. For example, this allows for a qualitative analysis of mixing phenomena. We refer the reader to fluid mechanics literature, e.g., (Mathur et al., 2007) for the underlying concepts, e.g., for details on mixing and the Lagrangian skeleton of turbulence.

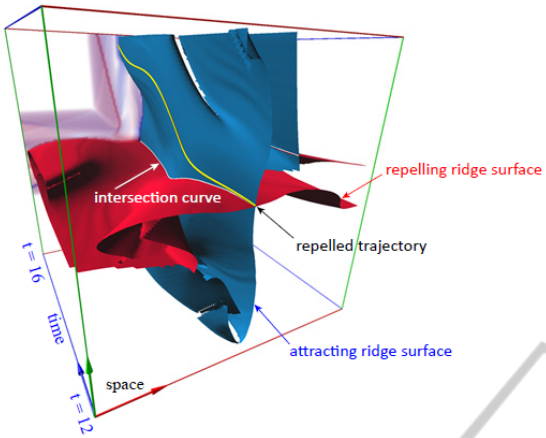

Figure 2: Space-time ridge surfaces in forward (red) and reverse (blue) finite-time Lyapunov exponent together with cross section at final time step (colored). The space-time intersection curve in the center (white) represents a hyperbolic trajectory. Traditional integration of the hyperbolic trajectory from the initial intersection is difficult due to exponential growth of error (yellow curve).

2 RELATED WORK

Work that is closely related to our objectives was discussed in the previous section, here we give a short overview of work that is in weaker context.

Many applications of vector field topology in fluid mechanics have been presented by Perry et al. (Perry and Chong, 1987). It was later introduced in visualization by Helman and Hesselink (Helman and Hesselink, 1989), (Helman and Hesselink, 1991) again in the context of flow fields. For details, we refer the reader to the work by Globus et al. (Globus et al., 1991), Asimov (Asimov, 1993), and Abraham and Shaw (Abraham and Shaw, 1992).

Vector field topology did also give rise to derived concepts and techniques. Examples are saddle connectors (Theisel et al., 2003) and boundary switch curves (Weinkauf et al., 2004a), both augmenting vector field topology by line-type features. Several approaches have been proposed for adopting the concepts to time-dependent vector fields, including the path line oriented topologies for 2D vector fields by Theisel et al. (Theisel et al., 2004) and Shi et al. (Shi et al., 2006), Galilean-invariant alternatives for critical points (Kasten et al., 2010), and basics for a Lagrangian vector field topology (Fuchs et al., 2010).

Separatrices and LCS are able to convey the structural and temporal organization of vector fields, however, at the same time, they suffer from this property; vector direction and magnitude are not represented, neither along these constructs, nor, and more importantly, in their vicinity. There are different approaches to overcome these drawbacks. Critical points are often visualized with glyphs representing the linearized flow. Another approach is to augment separatrices with arrows as presented by Weinkauf et al. (Weinkauf et al., 2004b). However, the most common approach in 2D and 3D vector field topology is to combine the separatrices with line integral convolution (LIC), e.g., see Weiskopf and Ertl (Weiskopf and Ertl, 2004). This vector field visualization with LIC can be either drawn between separatrices in the case of 2D vector fields, or on the separatrices themselves in the case of 3D vector fields. For time-dependent vector fields, this approach is not applicable because LIC visualizes transport along streamlines, i.e., instantaneous field lines, whereas LCS are usually obtained using true trajectories, i.e., from path lines. Therefore, other methods are required for visualizing the advection in the context of LCS, e.g., Shadden et al. (Shadden et al., 2005) advect particles. We exploit the fact that 2D time-dependent vector fields can be turned into 3D stationary vector fields by dimension lifting. Since the resulting domain is steady, streamlines are then equal to path lines, which allows us to use LIC. Texture-based methods (like LIC) have the advantage of avoiding the seed point positioning problem by conveying the field structure in a dense fashion. Since there is no intrinsic, predefined surface parametrization available, image-space oriented methods like (Laramee et al., 2003), (Wijk, 2003), and (Weiskopf and Ertl, 2004) are predestined for our task (we build on the latter one). More background information on texture-based vector field visualization can be found in the survey of (Laramee et al., 2004).

3 SPACE-TIME LCS VISUALIZATION

Our new visualization technique builds on the fact that time-dependent vector fields can be turned into stationary ones by treating time as additional dimension. This approach is common in the field of differential equations, where non-autonomous systems are made autonomous. Hence, 2D time-dependent vector fields $(u(x,y,t),v(x,y,t))^\top$ are converted into steady 3D vector fields $(u(x,y,t),v(x,y,t),1)^\top$, which we denote as space-time vector fields. All following steps of our algorithm (see Fig. 4) take place in this space-time domain. Since 2D path lines represent streamlines in space-time, we use 3D streamline integration over advection time T inside the space-time vector field to generate a flow map $\phi(x,y,t) \mapsto (x',y',t+T)^\top$. Then, for each time

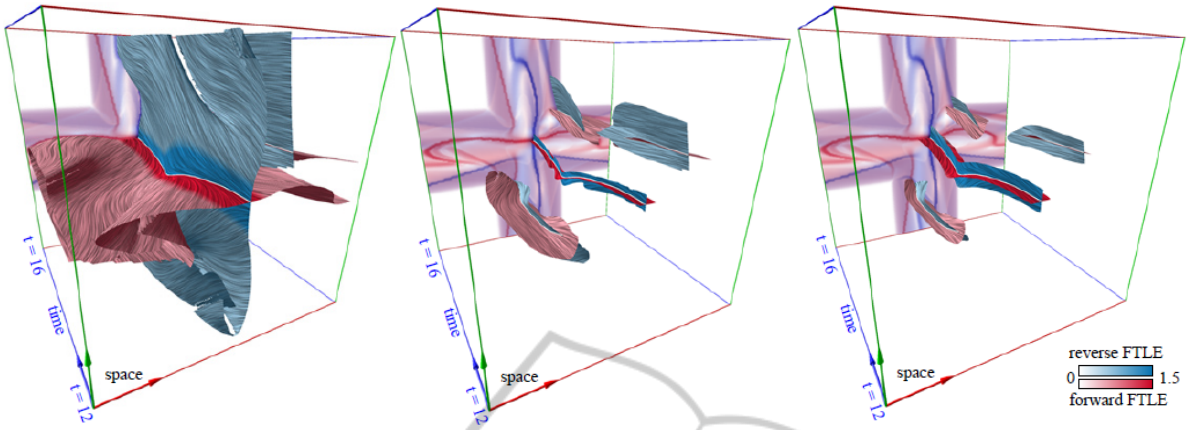

(a) (b) (c)

Figure 3: Building blocks for space-time LCS visualization, shown with the example from Sec. 5.1. Advection time for forward and reverse FTLE is $T = 4s$. (a) Space-time LIC qualitatively visualizes LCS dynamics: hyperbolic behavior is apparent. In addition, hyperbolicity is encoded by color saturation. A minimum FTLE value of 0.5 is used. (b) Intersection bands by clipping with complementary FTLE reduce occlusion but still provide context and convey structure of reverse FTLE. The minimum complementary FTLE value is 0.41. (c) Intersection bands by clipping with distance to intersection curves further reduces occlusion and provides the topological skeleton.

slice $\bar{t}$ of the space-time stack we compute the traditional 2D FTLE according to Haller (Haller, 2001) as $1/|T| \ln \sqrt{\lambda_{\max}[(\nabla_2 \phi(x,y,\bar{t}))^\top \nabla_2 \phi(x,y,\bar{t})]}$ with $\nabla_2 = (\partial/\partial x, \partial/\partial y, 0)^\top$ and major eigenvalue $\lambda_{\max}(\cdot)$. LCS are then extracted from the resulting stack of traditional 2D FTLE fields by ridge surface extraction, discussed in Section 3.1.

Due to the discussed material advection property of LCS, these surfaces represent stream surfaces in the space-time vector field, i.e., they are tangent to the space-time flow. This allows a direct application of LIC techniques, which we describe in Section 3.3. By this, LIC visualizes the dynamics of path lines along which the LCS are advected, and hence the dynamics within the LCS. As intersections of stream surfaces are streamlines, the space-time intersection of these LCS surfaces from forward and reverse FTLE represents a counterpart to hyperbolic trajectories. In Section 3.2, we address the investigation of these intersection curves in terms of hyperbolicity, again based on LCS. Restricting the LIC visualization to bands around the intersection curves comprises our second major contribution, detailed in Section 3.4.

3.1 Ridge Surface Extraction

We extract the ridge surfaces from the stack of 2D FTLE fields as height ridges (Eberly, 1996) of codimension one from the 3D space-time FTLE field, according to Sadlo and Peikert (Sadlo and Peikert, 2009). We follow this approach to avoid the problems that would arise from stitching of the individual ridge curves from the 2D FTLE fields. Furthermore, ridges are typically non-manifold, which would cause further issues. Since Eberly's formulation (Eberly, 1996) is local and relies on higher-order derivatives, it is subject to erroneous solutions. It is therefore common practice to apply filtering and we follow the filtering process described by Sadlo and Peikert (Sadlo and Peikert, 2007): since only sufficiently "sharp" FTLE ridges represent LCS, ridge regions where the modulus of the eigenvalue of the Hessian is too low are suppressed. Further, we require a minimum FTLE value, hence requiring a minimum separation strength of the LCS. Finally, to suppress small ridges, we filter the ridge surfaces by area. As described in (Sadlo and Peikert, 2007), we also use a least-squares approach to prevent noise amplification during estimation of the gradient and Hessian. Figure 2 shows examples of ridges extracted from a stack of forward and reverse-time FTLE: repelling LCS (ridges in forward FTLE) colored red and attracting ones (ridges in reverse FTLE) blue. The space-time structure of the field is revealed including the intersection curves. However, this does not convey hyperbolicity aspects, e.g., it does not disambiguate intersection curves representing strong hyperbolic trajectories from weak hyperbolic ones. This motivates the visualization of hyperbolicity on LCS.

3.2 Visualizing Hyperbolicity

To help the user in the investigation of hyperbolic effects, and hyperbolic trajectories in partic-

ular, we map hyperbolicity to saturation, shown in Fig. 3a. We have chosen the hyperbolicity definition by Haller (Haller, 2000), i.e., the sign of the determinant of the velocity gradient of the original 2D vector field at the respective space-time location. One can see how this technique not only reveals the presence of hyperbolicity but also allows for the interpretation of the hyperbolic regions around the intersection curves. To examine hyperbolicity more precisely, we introduce a novel technique to visualize LCS dynamics in the next section.

3.3 Visualizing LCS Dynamics

The LCS in our space-time FTLE field are present as ridge surfaces and to fully capture the spatial variation of their dynamics they lend themselves to dense texture-based visualization such as LIC. Since LCS lack intrinsic surface parametrization and need to be analyzed in overview scales as well as in local detail, image-space oriented approaches are predestined to visualize the space-time structure. We use the hybrid physical/device-space LIC approach by Weiskopf and Ertl (Weiskopf and Ertl, 2004), which relies on particle tracing computed in the physical space of the object and in the device space of the image plane at the same time. The LIC pattern is based on the tangential part of the vectors attached to our surfaces. This dual-space approach combines the advantages of image-space methods with frame-to-frame coherence and avoids inflow issues at silhouette lines. For a detailed description of this visualization technique, we refer to the original paper.

In the context of our visualization of LCS dynamics, the goal is to visualize the space-time direction of the vector field. Hence, we normalize the space-time vectors during LIC computation to obtain LIC line patterns of uniform length for optimal perception. In contrast to traditional spatial LIC, we retain the visual encoding of velocity magnitude in the form of surface orientation in space-time. For example, small angles between surface normal and the time axis indicate high speed.

Figure 3a exemplifies the method again on the same data set. It is apparent how this technique conveys the time-dependent dynamics within LCS. Combining it with the saturation-based visualization of hyperbolicity (Section 3.2) supports the identification of hyperbolic intersection curves and still provides the LCS dynamics context. Since LCS are often convoluted, they typically exhibit many intersections that are, however, often occluded. We address this problem by the building block described next: the restriction of the technique to regions around space-time LCS intersection curves. At the same time, this approach explicitly addresses the analysis of the intersection curves.

3.4 LCS Intersection Bands

Even in the simple example shown so far, it is obvious that occlusion tends to be a problem in space-time visualization of LCS. To address this and to provide a method for analyzing intersection curves of LCS at the same time, we introduce two complementary approaches that have proven valuable in our experiments, both restricting the presented visualization to bands around the LCS intersection curves.

As discussed in Section 3.1, a common approach is to filter FTLE ridges by prescribing a minimum FTLE value. This way, the visualization is restricted to important LCS, i.e., those representing strong separation. This filter is applied to ridges in both forward and reverse FTLE fields. If we additionally prescribe a minimum value for the complementary FTLE, i.e., the reverse in case of forward FTLE ridges and the forward in case of reverse FTLE ridges, one typically restricts the visualization to bands around the intersection curves, shown in Fig. 3b. This technique has the advantage that the profile of the complementary FTLE field is conveyed, allowing qualitative interpretation of the interplay of LCS. Furthermore, it often features additional bands that do not exhibit LCS intersections. They are generated if FTLE ridges are located in regions of high complementary FTLE. These additional bands are still of interest: the respective regions exhibit both high forward and reverse-time FTLE. Additionally, these bands may connect to other bands that feature intersection curves and hence convey the overall organization of the LCS. A drawback of this approach, however, is that the bands may get too narrow for appropriate LIC visualization or too wide to sufficiently reduce occlusion.

Therefore, we propose, as an alternative, to restrict the LCS to the neighborhood of their intersection curves. To avoid numerical issues, we first omit regions where the LCS intersect at small angle.

Furthermore, a minimum length of the intersection curves is required to obtain significant visualizations. The remaining intersection curves are then used for distance computation, leading to a distance field on the LCS that is then used for clipping. Figure 3c shows an example: the dynamics of the LCS is well depicted by LIC and at the same time occlusion is substantially reduced, allowing for the analysis of the intersection curves with respect to LCS dynamics and hyperbolicity. Since the resulting bands can still be too narrow due to perspective foreshortening, we

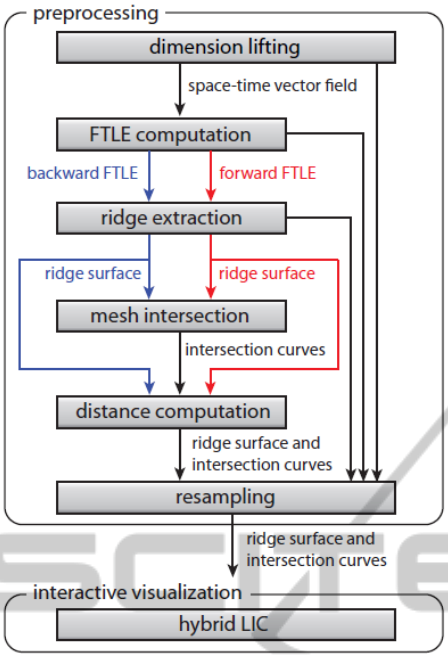

Figure 4: Overview of our technique, accompanied by the data that are passed between the stages of the pipeline.

also support depth-corrected width of the bands described in Section 4.2.

To sum up, these clipping approaches result in visualizations that can be seen as an extended topological skeleton of time-dependent flow. Note that we use equal thresholds for forward and reverse-time FTLE ridge filtering as well as for complementary FTLE band clipping, for ensuring consistent visualization. Finally, we would like to point out the similarity to saddle connectors (Theisel et al., 2003), although our approach resides in space-time, whereas saddle connectors visualize 3D steady vector fields.

3.5 Combined Visualization

Our system allows the user to interactively switch on and off the clipping for intersection bands. When clipping is enabled, the remaining choice is between complementary FTLE and distance-based intersection bands. Depth-correction of intersection band width is always enabled. In summary, only three different modes (no clipping, complementary clipping, distance-based clipping) are required to cover the visualization needs.

4 IMPLEMENTATION

This section details the implementation of the different building blocks of our technique as well as modifications to existing approaches. The pipeline shown in Fig. 4 gives an overview of the steps and provides information about the data that are exchanged between different stages of the pipeline.

4.1 Preprocessing

Several steps in our technique are performed in a preprocessing phase, once per data set.

The original data set is given as a series of time steps of a 2D vector field. To create the stationary space-time 3D vector field, we apply dimension lifting, i.e., the time series of the 2D vector field are stacked and the time dimension is treated as additional third dimension. This space-time vector field is used to compute the 3D space-time FTLE field for forward and reverse time direction. Using this FTLE field, ridge surfaces are extracted. A detailed description of the ridge extraction method is given by Sadlo and Peikert (Sadlo and Peikert, 2007).

The ridge surface meshes from forward and reverse–time FTLE are intersected to obtain the intersection curves. Once the geometry of all intersection curves is obtained, a distance field is computed that holds the distance of ridge surface vertices to the nearest intersection curve. Next, we compute vertex-based normals, which are used for shading in the interactive visualization. During this process, normals are reoriented if necessary; however, since ridge surfaces are not necessarily orientable, we may not succeed for all normals. Remaining inconsistencies for the normals are treated during interactive visualization using a shader. Finally, the space-time flow vectors are sampled at the vertex locations of the ridge surface mesh. This resampling is independent of the FTLE sampling grid, allowing for acceleration methods (Garth et al., 2007), (Sadlo and Peikert, 2007), and (Hlawatsch et al., 2011). Distance values, normals, resampled flow vectors, and additional scalars like FTLE values, hyperbolicity, and the minor eigenvalue of the Hessian (see Section 3.1) are attached to the ridge surface mesh that is then passed to the interactive visualization stage.

4.2 Interactive Visualization

The core of our interactive visualization is based on hybrid physical/device-space LIC (Weiskopf and Ertl, 2004) to create line-like texture on the ridge surfaces.

During rendering of the space-time ridge surfaces, we apply Phong illumination to enhance visibility and perception of the geometry. Since the ridge surfaces may be non-orientable, we have to ensure that local

normal vectors are consistently oriented in order to avoid shading artifacts. Therefore, we make normal orientation consistent during fragment processing using the dot product between normal and view vector. This prevents inconsistent shading due to normal interpolation; however, ridge surfaces may still appear rippled. This happens because of FTLE aliasing effects at strong and sharp ridges, where very high FTLE gradients are present. To compensate for this, we correct the normals to be perpendicular to the space-time vector field and hence to its LCS during fragment processing.

We handle occlusion by attaching additional data (regular FTLE, complementary FTLE, distance to nearest intersection curve) obtained during the preprocessing stage (see Section 4.1) to each vertex of the ridge surface mesh and upload this data as additional texture coordinates to the GPU. Fragments that do not meet the filtering criteria are discarded. All thresholds used in this process are adjustable in real-time by the user. In addition to user controlled clipping, we adjust the width of our LCS intersection bands if they are clipped by the distance to the nearest intersection curve. We adjust the clipping threshold based on distance to the camera position. This results in intersection bands with constant image-space width, which reduces occlusion of intersection bands that are close to the camera. At the same time, intersection bands that are farther away are enlarged, which improves visibility of the LIC pattern.

5 RESULTS

We apply the presented methods to different data sets. The first two data sets are synthetic, whereas the third is created by CFD simulation, and the fourth is obtained by remote sensing of ocean currents.

Our implementation was tested on a PC with an Intel Core Quad CPU (2.4 GHz), 4 GB of RAM and an NVIDIA GeForce 275 GPU with 896 MB of dedicated graphics memory. Each of the presented data sets is visualized at interactive rates. Since our implementation is based on the approach presented by Weiskopf and Ertl (Weiskopf and Ertl, 2004), it shows the same performance behavior—we refer to their paper for a detailed performance analysis.

A bounding box of the domain helps the user to navigate and orientate in space-time. This bounding box is color coded—the time dimension is indicated by a blue axis while the two spatial dimensions have a red and green axis, respectively. The last time step of the space-time region of interest is located at the back end of the bounding box which shows the FTLE field

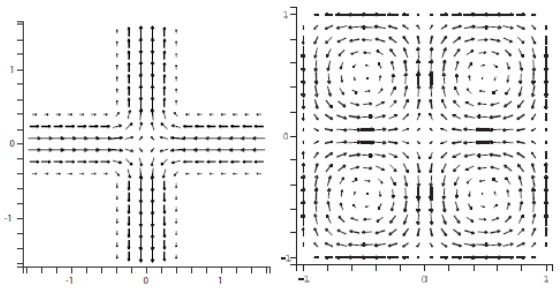

(a) (b)

Figure 5: (a) Gyre Saddle example at $t = 0$. (b) Quad Gyre example at $t = 0$.

as a color–coded texture. In this texture, FTLE values are mapped to saturation, with full saturation mapping to the highest FTLE value. There, we use the same color-coding as for the space-time ridge surfaces.

5.1 Oscillating Gyre Saddle

The synthetic vector field that we use as an example in this section is due to Sadlo and Weiskopf (Sadlo and Weiskopf, 2010). It exhibits a non-linear saddle (Fig. 5a) that oscillates between the locations $(0.25, 0.25)$ and $(-0.25, -0.25)$ at a period of $\tau = 4$. Please refer to Fig. 1, Fig. 2, and Fig. 3 for resulting visualizations. To sum up, it exhibits a strongly hyperbolic intersection curve visualized in Fig. 1 (right) and several non-hyperbolic ones. This is consistent with the Eulerian picture (Fig. 5a) showing distinguished saddle behavior at its center. As mentioned by Sadlo and Weiskopf (Sadlo and Weiskopf, 2010), there are other ridges due to shear processes. These are of inferior importance for mixing and cannot give rise to hyperbolic trajectories, i.e., their LIC patterns do not show hyperbolic behavior. Note that we filter FTLE ridges to show the strongest and largest LCS. Supressing weaker ridges simplifies the resulting visualization which we use for depicting purposes.

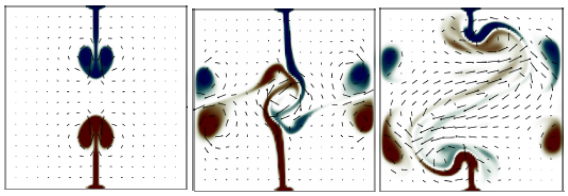

(a) (b) (c)

Figure 6: Three time steps of the buoyant plume example, color indicates temperature (red maps to high temperature, blue to low temperature). (a) Two plumes build up and travel toward each other in vertical direction. (b) After collision, two new plumes are created that travel toward the walls. (c) After collision with the side walls.

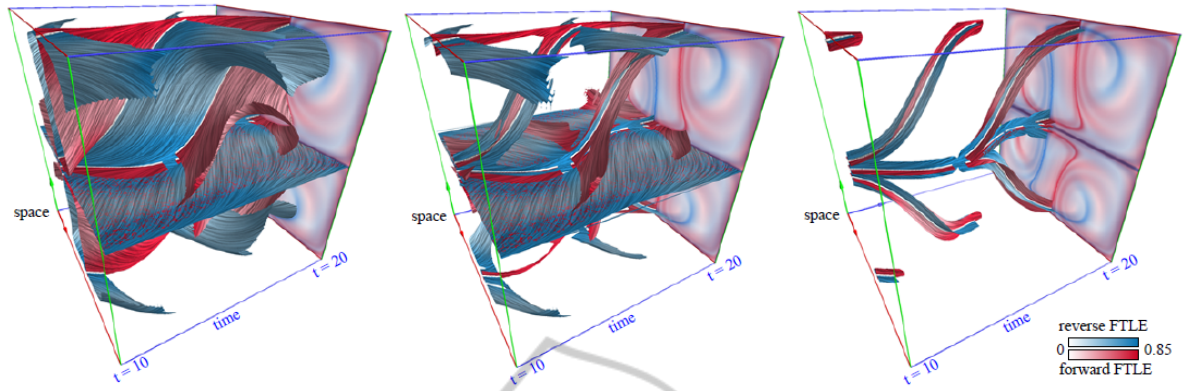

(a) (b) (c)

Figure 7: Quad-Gyre example. The advection time for forward and reverse FTLE is $T = 7.5s$. (a) Full visualization of forward and reverse LCS. A lower FTLE threshold of 0.4 is used. (b) Visualization restricted to complementary FTLE bands. Minor artifacts appear due to aliasing effects of forward and reverse FTLE. The minimum complementary FTLE value is 0.19. (c) Restriction to distance-based LCS intersection bands reveals the topological space-time skeleton.

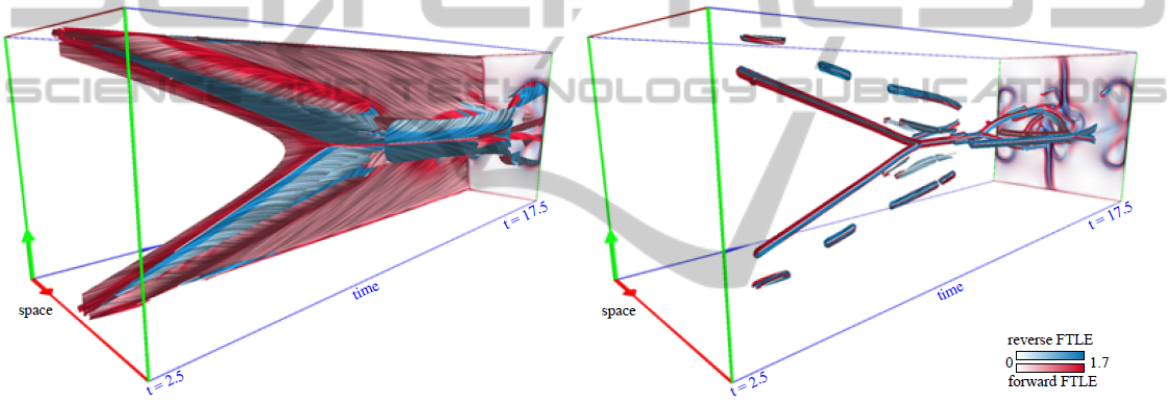

(a) (b)

Figure 8: Buoyant plumes example. The advection time for forward and reverse FTLE is $T = 1.5s$. (a) Full visualization of forward and reverse LCS. The dynamics of the two plumes is apparent in the first part of the examined time interval. A lower FTLE threshold of 0.87 is used. (b) LCS intersection bands clipped by distance, revealing the skeleton.

5.2 Quad Gyre

The double gyre example was introduced by Shadden et al. (Shadden et al., 2005) to examine FTLE and LCS, and to compare them to vector field topology. It consists of two vortical regions separated by a straight separatrix that connects two saddle-type critical points: one oscillating horizontally at the upper edge and the other synchronously oscillating horizontally along the lower edge. This is a prominent example where the vector field topology result substantially differs from LCS. This data set is temporally periodic. To avoid boundary issues, we use a larger range of field, resulting in four gyres. As proposed by Shadden et al., we use the configuration $\varepsilon = 1/4$, $\omega = \pi/5$, and $A = 1/10$. Figure 5b shows a plot at $t = 0$ for these parameters.

Rendering the quad gyre without clipping (Fig. 7a) results in space-time ridges that heavily occlude each other. Please note that the $y = 0$ plane represents an LCS in both forward and reverse direction, which results in z-fighting. Nevertheless, the LIC line pattern is consistent in that region due to the image-based LIC technique. Reducing occlusion by clipping with the complementary FTLE (Fig. 7b) removes parts of the ridge surfaces, while preserving the context of the bands. Note, for example, that the red bands are connected at the upper edge of the domain and hence are part of the same LCS. If we clip the space-time ridge surfaces by distance to their intersection curves (Fig. 7c), occlusion is even more reduced, but less context is conveyed. However, this technique especially pays off in data sets with complex space-time dynamics, since the topological skeleton is well visi-

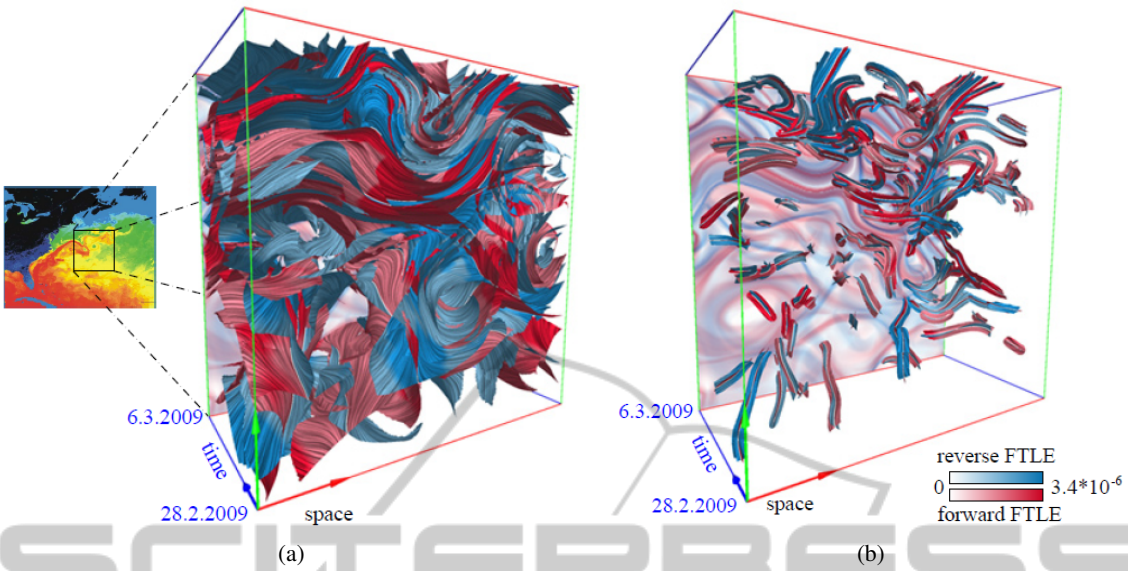

Figure 9: OSCAR example. The advection time for forward and reverse FTLE is $T = 25$ days. The small map on the left hand side shows the atlantic ocean and the east coast of North America. It gives a frame of reference for our visualization results and exemplifies the prevalent mixing due to the gulf stream. Please note that this map does not show flow but rather water temperature mapped to colors and that it was generated outside of the investigated time interval. (a) Full visualization of forward and reverse LCS. A lower FTLE threshold of 9×10^{-7} is used. Flow around several intersection curves shows strong hyperbolic behavior. (b) LCS intersection bands clipped by distance.

ble from most views. In all images, hyperbolicity is visualized by mapping it to the saturation of the ridge surface color. It can be seen that it readily guides attention to hyperbolic LIC patterns. As in the results by Sadlo and Weiskopf (Sadlo and Weiskopf, 2010), we identify a hyperbolic trajectory at the center of the data set.

5.3 Buoyant Plumes

This data was obtained by a CFD simulation of buoyant 2D flow. A square container was modeled with a small heated region at its bottom wall and a small cooled region at its top wall. Figure 6 illustrates the flow. Two plumes are developed, a hot one rising to the top and a cold one moving in reverse direction to the bottom. They then collide at the center and give rise to two new plumes traveling horizontally toward the side walls. As they approach the walls, they both split and produce plumes traveling in vertical direction. From that point on, the regular behavior is replaced by increasingly turbulent flow behavior.

Figure 8a shows the visualization of both forward- and reverse-time FTLE ridges. There is no clipping applied for this image but saturation already guides to the hyperbolic regions, however, many of them are occluded. In Fig. 8b, the distance-based LCS intersection bands nicely visualize the hyperbolic mechanisms. One can see how the two plumes approach each other and merge, then divide and later give rise to turbulent flow. We finally identify several strong hyperbolic regions toward the end of the examined time interval. The multitude of hyperbolic regions approves the observation of strong buoyant mixing. The high intricacy and topological complexity of turbulent buoyant flow reflects in our visualization.

5.4 OSCAR

Ocean Surface Currents Analyses Real-time (OSCAR) (Bonjean and Lagerloef, 2002) is a project to calculate ocean surface velocities from satellite data. The OSCAR product is a direct computation of global surface currents using satellite sea surface height, wind, and temperature. The OSCAR analyses have been used extensively in climate studies, such as for ocean heat storage and phytoplankton blooms.

We applied our technique to the gulf stream at the east coast of North America. We thereby focused on a strong hyperbolic LCS system involved in mixing (Fig. 9a). As expected, our technique revealed a complex Lagrangian skeleton of turbulence (Mathur et al., 2007), shown in Fig. 9a. Our LIC patterns allow a direct and qualitative inspection of the LCS with respect to hyperbolic mechanisms and mixing. Whereas many regions in the OSCAR data set exhibited inferior hyperbolic behavior, it is prominent in the selected region. Again, the LCS intersection

bands dramatically reduce occlusion while still conveying topological structure and hyperbolic dynamics, see Fig. 9b. Following the LIC line patterns along the temporal axis directly conveys the action of the flow in terms of mixing, i.e., thinning and folding.

6 CONCLUSIONS

We have presented an approach for the visualization and analysis of the dynamics in LCS of time-dependent 2D vector fields. Compared to traditional approaches, we do not restrict the investigation of LCS to their geometric shape. We extend the visualization by allowing the user to analyze the intrinsic dynamics of LCS in terms of stretching and compression, in particular along hyperbolic trajectories. These dynamics are visualized by space-time LIC on space-time ridge surfaces of the 2D FTLE.

Occlusion problems due to convoluted and heavily intersecting LCS are reduced by clipping of the LCS, providing LCS intersection bands. Clipping can be based on the distance to the hyperbolic trajectories and on forward and reverse FTLE to suppress less important regions. A major numerical aspect of our method is the avoidance of the difficult direct integration of hyperbolic trajectories, we intersect FTLE ridge space-time surfaces instead. Still, the growth of the respective space-time streak manifolds is conveyed by the LIC.

Finally, we have demonstrated the applicability of our method with several synthetic and real-world data sets, also in the context of turbulent flow analysis, a topic of ongoing research. In future work, we plan to extend our technique to 3D time-dependent vector fields, i.e., investigate intersection curves of LCS and the surfaces they span over time.

ACKNOWLEDGEMENTS

The first author and fourth author thank the German Research Foundation (DFG) for financial support within SFB 716 / D.5 at University of Stuttgart. The second author thanks DFG for financial support within the Cluster of Excellence in Simulation Technology (EXC 310/1), and SFB-TRR 75 at University of Stuttgart.

REFERENCES

Abraham, R. H. and Shaw, C. D. (1992). *Dynamics, the Geometry of Behavior. 2nd ed.* Addison-Wesley.

Asimov, D. (1993). Notes on the topology of vector fields and flows. Technical Report RNR-93-003, NASA Ames Research Center.

Bonjean, F. and Lagerloef, G. (2002). Diagnostic model and analysis of the surface currents in the tropical pacific ocean. *Journal of Physical Oceanography*, 32(10):2938–2954.

Eberly, D. (1996). *Ridges in Image and Data Analysis. Computational Imaging and Vision*. Kluwer Academic Publishers.

Fuchs, R., Kemmler, J., Schindler, B., Sadlo, F., Hauser, H., and Peikert, R. (2010). Toward a Lagrangian vector field topology. *Computer Graphics Forum*, 29(3):1163–1172.

Garth, C., Gerhardt, F., Tricoche, X., and Hagen, H. (2007). Efficient computation and visualization of coherent structures in fluid flow applications. *IEEE Transactions on Visualization and Computer Graphics*, 13(6):1464–1471.

Globus, A., Levit, C., and Lasinski, T. (1991). A tool for visualizing the topology of three-dimensional vector fields. In *Proc. of IEEE Visualization*, pages 33–41.

Haller, G. (2000). Finding finite-time invariant manifolds in two-dimensional velocity fields. *Chaos*, 10(1):99–108.

Haller, G. (2001). Distinguished material surfaces and coherent structures in three-dimensional fluid flows. *Physica D Nonlinear Phenomena*, 149(4):248–277.

Helman, J. and Hesselink, L. (1989). Representation and display of vector field topology in fluid flow data sets. *IEEE Computer*, 22(8):27–36.

Helman, J. and Hesselink, L. (1991). Visualizing vector field topology in fluid flows. *IEEE Computer Graphics and Applications*, 11(3):36–46.

Hlawatsch, M., Sadlo, F., and Weiskopf, D. (2011). Hierarchical line integration. *IEEE Transactions on Visualization and Computer Graphics*, 17(8):1148 –1163.

Ide, K., Small, D., and Wiggins, S. (2002). Distinguished hyperbolic trajectories in time-dependent fluid flows: Analytical and computational approach for velocity fields defined as data sets. *Nonlinear Processes in Geophysics*, 9(3/4):237–263.

Kasten, J., Hotz, I., Noack, B., and Hege, H.-C. (2010). On the extraction of long-living features in unsteady fluid flows. In Pascucci, V., Tricoche, X., and Terny, J., editors, *Topological Methods in Data Analysis and Visualization. Theory, Algorithms, and Applications.*, Mathematics and Visualization, pages 115–126. Springer.

Laramee, R. S., Hauser, H., Doleisch, H., Vrolijk, B., Post, F. H., and Weiskopf, D. (2004). The state of the art in flow visualization: Dense and texture–based techniques. *Computer Graphics Forum*, 23(2):203–221.

Laramee, R. S., Jobard, B., and Hauser, H. (2003). Image space based visualization of unsteady flow on surfaces. In *Proc. IEEE Visualization*, pages 131–138.

Lekien, F., Coulliette, C., Mariano, A. J., Ryan, E. H., Shay, L. K., Haller, G., and Marsden, J. E. (2005). Pollution release tied to invariant manifolds: A case study for

the coast of Florida. *Physica D Nonlinear Phenomena*, 210(1):1–20.

Mathur, M., Haller, G., Peacock, T., Ruppert-Felsot, J. E., and Swinney, H. L. (2007). Uncovering the Lagrangian skeleton of turbulence. *Physical Review Letters*, 98(14):144502.

Perry, A. E. and Chong, M. S. (1987). A description of eddying motions and flow patterns using critical-point concepts. *Annual Review of Fluid Mechanics*, 19:125–155.

Sadlo, F. and Peikert, R. (2007). Efficient visualization of Lagrangian coherent structures by filtered AMR ridge extraction. *IEEE Transactions on Visualization and Computer Graphics*, 13(5):1456–1463.

Sadlo, F. and Peikert, R. (2009). Visualizing Lagrangian coherent structures and comparison to vector field topology. In *Topology-Based Methods in Visualization II*, pages 15–30.

Sadlo, F., Rigazzi, A., and Peikert, R. (2011). Time–dependent visualization of Lagrangian coherent structures by grid advection. In *Topological Methods in Data Analysis and Visualizationc (Proceedings of TopoInVis 2009)*, pages 151–165. Springer.

Sadlo, F., Üffinger, M., Ertl, T., and Weiskopf, D. (2012). On the finite–time scope for computing Lagrangian coherent structures from Lyapunov exponents. In *Topological Methods in Data Analysis and Visualization II (Proceedings of TopoInVis 2011)*, pages 269–281. Springer.

Sadlo, F. and Weiskopf, D. (2010). Time–dependent 2D vector field topology: An approach inspired by Lagrangian coherent structures. *Computer Graphics Forum*, 29(1):88–100.

Shadden, S., Lekien, F., and Marsden, J. (2005). Definition and properties of Lagrangian coherent structures from finite-time Lyapunov exponents in two-dimensional aperiodic flows. *Physica D Nonlinear Phenomena*, 212(3):271–304.

Shi, K., Theisel, H., Weinkauf, T., Hauser, H., Hege, H.-C., and Seidel, H.-P. (2006). Path line oriented topology for periodic 2D time–dependent vector fields. In *Proc. Eurographics / IEEE VGTC Symposium on Visualization*, pages 139–146.

Theisel, H., Weinkauf, T., Hege, H.-C., and Seidel, H.-P. (2003). Saddle connectors - An approach to visualizing the topological skeleton of complex 3D vector fields. In *Proc. IEEE Visualization*, pages 225–232.

Theisel, H., Weinkauf, T., Hege, H.-C., and Seidel, H.-P. (2004). Stream line and path line oriented topology for 2D time–dependent vector fields. In *Proc. IEEE Visualization*, pages 321–328.

Weinkauf, T., Theisel, H., Hege, H.-C., and Seidel, H.-P. (2004a). Boundary switch connectors for topological visualization of complex 3D vector fields. In *Proc. Joint Eurographics - IEEE TCVG Symposium on Visualization (VisSym '04)*, pages 183–192.

Weinkauf, T., Theisel, H., Hege, H.-C., and Seidel, H.-P. (2004b). Topological construction and visualization of higher order 3D vector fields. In *Computer Graphics Forum*, pages 469–478.

Weiskopf, D. and Ertl, T. (2004). A hybrid physical/device-space approach for spatio-temporally coherent interactive texture advection on curved surfaces. In *Proc. Graphics Interface*, pages 263–270.

Wiebel, A., Tricoche, X., Schneider, D., Jaenicke, H., and Scheuermann, G. (2007). Generalized streak lines: Analysis and visualization of boundary induced vortices. *IEEE Transactions on Visualization and Computer Graphics*, 13(6):1735–1742.

Wijk, J. J. V. (2003). Image based flow visualization for curved surfaces. In *Proc. IEEE Visualization*, pages 123–130.